A comparison of two-fluid and one-fluid dust solvers for dusty, supersonic turbulence

by

Narges Vadood

A thesis submitted to the

School of Graduate Studies

to fulfill the requirements for the degree of

Master of Science.

Supervisor: Terrence Tricco

Memorial University of Newfoundland

St. John's, NL, Canada

November 21, 2024

Abstract

Dust is an important observational tracer of gas in molecular clouds and different dust solvers have led to conflicting conclusions about dust distributions. For this reason, We model 3 and 10 μm dust grains in supersonic, turbulent molecular cloud conditions to compare two different numerical methods solving dust coupled to gas through a drag term. One method models dust and gas as two separate species (two-fluid) and the other the combination of dust and gas as a single mixture (one-fluid). Simulations are performed in a 3D periodic box using the Phantom code. The gas probability distributions are consistent with a log-normal distribution for both methods and grain sizes. The dust distributions are different in the two methods, showing discrepancies especially in low densities. The most significant difference between the two methods is in the dust-to-gas ratio distributions. Both methods peak at the mean dust-to-gas ratio of 0.01, but the two-fluid method has wider distributions than the one-fluid method suggesting excess dust concentration in dense filaments. Filaments are where the one-fluid method results are most accurate, but the narrowing of the distribution is also caused by the one-fluid limiter used to maintain the terminal velocity approximation. This artificially makes the mixture more coupled in low-density regions. Our overall conclusion is that both methods are viable for the study of dust in molecular clouds, but that the correct method should be chosen based on the Stokes number regime of the calculation to avoid numerical artefacts.

Contents

List of Figures

List of Tables

Chapter 1

Introduction

Dust plays a crucial role in the dense interstellar medium (ISM) of our Galaxy, serving as the primary source of opacity and light scattering. Dense molecular clouds are regions in space with relatively high densities of molecular hydrogen, with mean densities of $n_{H_2} \sim 100$ –1000 cm^{-3}, compared to other types of interstellar medium (ISM) (Snow and McCall, 2006; Ballesteros-Paredes et al., 2020; Colman et al., 2024). These clouds have relatively low temperatures, usually around 10 K, and can span large regions, sometimes hundreds of light years across.

Dense molecular clouds play a significant role in the life cycle of the ISM, acting as a reservoir of molecular gas that can eventually collapse under gravity to form new stars in the denser regions. These clouds are primarily composed of molecular gas (99%), and most of that is molecular hydrogen which is difficult to detect directly (Habart et al., 2005). The second most abundant element is helium, which is a noble

gas and invisible. The second most abundant molecule is CO, which has rotational transitions that are easily excited at typical molecular clouds temperatures and densities, making it useful as a tracer of hydrogen in cold molecular clouds to investigate molecular cloud properties (Solomon et al., 1979).

These clouds also contain solid dust grains composed of silicates and carbonaceous materials of sizes from a few micrometers to a few nanometers (Mathis et al., 1977), which account for about 1% of the mass in molecular clouds (Bohlin et al., 1978). For a review on interstellar dust grains' properties, see Draine (2003). Historically, interstellar dust was first recognized for its ability to obscure starlight. Subsequently, dust was used as a tracer for studying cold molecular clouds (Lada et al., 1994), providing more detailed and robust measurements of cloud sizes, masses, and internal structures compared to CO observations of the same regions within the Milky Way (Goodman et al., 2009). The advantage of using dust over molecular lines lies in the fact that dust grains do not require a minimum density to be detectable and remain effective at high densities, whereas molecular lines can become problematic.

More fundamentally, dust grains play several critical roles in controlling the physics and chemistry of the interstellar medium (Draine, 2011). One significant chemical effect is that dust grains provide surfaces on which hydrogen atoms can come together and react to form molecular hydrogen (H_2). In the cold, sparse environment of interstellar space, gas-phase reactions are too slow to efficiently produce H_2. However, dust grains act as catalysts, facilitating the reaction by bringing hydrogen atoms into

close proximity on their surfaces and allowing them to bond and form H_2 molecules. As a physical effect, dust grains exposed to ultraviolet starlight can significantly heat the gas by releasing electrons (referred to as "photoelectrons"). When these electrons are ejected from dust grains, they carry kinetic energy, which is then transferred to the surrounding gas, resulting in its heating. Conversely, infrared emission from dust grains serves as an important cooling mechanism, particularly in dense regions. Dust grains absorb energy from their surroundings, and as they warm up, they can lose this energy by emitting it as infrared radiation.

Molecular clouds exhibit high turbulence (Solomon et al., 1987; Larson, 1981). Regardless of the underlying mechanisms driving it, turbulence can lead to the accumulation of gas in filaments and cause the formation of complex, filamentary shapes, which resemble the intricate, irregular forms observed in molecular clouds (Schneider et al., 2011). It is a question on whether turbulence can drive variations in the local dust-to-gas ratio. If so, then this would have implications on derived cloud masses, as the calibration of H_2 column density to integrated CO intensity (X-factor) is often derived using dust extinction (Pineda et al., 2008; Kong et al., 2015; Liseau et al., 2015; Lada and Dame, 2020; Lewis et al., 2022).

Several numerical studies have investigated the dynamics of dust grains within cold, turbulent molecular clouds, revealing variations in dust concentration. Hopkins and Lee (2016) use meshless finite mass (MFM) (Hopkins, 2015) where two separate fluids of gas and dust are modeled using two types of particles, and they report a

variation in dust concentration by more than a factor of 1000 for dust grains larger than 0.01 μm with their simulation setup. They observed the emergence of dust filaments even in the absence of gas filaments. In Mattsson et al. (2019a), the gas is considered on a uniform Cartesian grid (Eulerian approach), while the dust fluid is handled using inertial particles (Lagrangian approach). Mattsson et al. (2019a) report large dust-to-gas ratio variations for grain sizes larger than 1 μm, and Mattsson et al. (2019b) show small-scale clustering (increasing the local grain density by at least a factor of a few) for nanometer-sized grains. These findings indicate that dust grains decouple from the gas at these sizes and no longer trace the gas.

In contrast, Tricco et al. (2017) only report significant decoupling only for dust grains larger than 10 μm, with 0.1 μm dust grains remaining highly coupled to the gas distribution. This is contrast to the results found by Hopkins and Lee (2016) and Mattsson et al. (2019a). The key difference between these results is that Tricco et al. (2017) track the evolution of the barycenter of mass between the gas and the dust using smoothed particle hydrodynamics (SPH) simulations. The full one-fluid system of equations governing gas and dust dynamics is mathematically equivalent to the set of equations in the two-fluid formalism, but involves a change of variables that allows tracking the evolution of the mixture's barycenter, relative velocity difference, and dust concentration. This has been further simplified using the diffusion approximation (Price and Laibe, 2015), which is grounded in the terminal velocity approximation (Youdin and Goodman, 2005).

While suitable for well-coupled dust grains in molecular clouds (small grains in dense environments), the one-fluid diffusion approximation is inadequate for larger grains as it underestimates the velocity difference between the dust and gas. This means that numerical artefacts may appear for large dust grains or in low density environments where the dust stopping time exceeds the local dynamical time. The issue with the two-fluid results, where gas and dust are modeled separately, is that the dust is pressureless. Federrath et al. (2010) demonstrated that pressureless tracer particles in simulations of supersonic turbulence fail to accurately represent dynamics, resulting in numerical artifacts. These artifacts manifest as exaggerated concentration in high-density regions and almost complete absence in underdense regions. Moreover, Laibe and Price (2012) established that simulations of two-fluid dust and gas mixtures require sufficient gas resolution to adequately resolve the lengthscale over which dust grains begin co-moving with the gas (dust "stopping length").

What is needed is a comparative study where the same simulation is performed side-by-side using the two-fluid and one-fluid dust methods to determine the conditions in which the two methods agree on their solutions for molecular clouds. Commerçon et al. (2023) has recently performed this type of study using the grid-based code Ramses (Teyssier, 2002). For the two-fluid method, the dust is treated as Lagrangian particles while the gas dynamics are computed on an Eulerian grid. They find similar results as previous studies. For two-fluid simulations, they find artificial dust trapping in high-density regions, with the maximum dust enrichment affected

by the gas resolution. For their one-fluid simulations, they find that the terminal velocity approximation is well suited for < 10 μm dust grains inside dense filaments, but does not accurately capture dust dynamics in low density regions. They conclude that the numerical properties of these two methods needs further study.

Our goal is to evaluate the effectiveness of the two-fluid and one-fluid numerical methods for the evolution of dust and gas mixtures in supersonic, turbulent molecular clouds. Our work is very similar to that of Commerçon et al. (2023), with a key difference that we include a limiter on the stopping time for the one-fluid method. Ballabio et al. (2018) recommend this limiter to ensure the equations of motion remain valid within the terminal velocity approximation, particularly in low-density areas where the stopping time might surpass the dynamical time (Courant time). We specifically choose dust grain sizes and molecular cloud conditions to try to meet the numerical requirements of both methods. Everything is performed in the Phantom SPH code (Price et al., 2018), so that any differences found in our results can be attributed entirely to the choice of dust solver.

The thesis is organized as follows. The continuum equations described in Chapter 2. The numerical methods is discussed in Chapter 3. The simulation conditions and results are presented in Chapter 4. Conclusions are given in Chapter 5.

Chapter 2

Continuum equations

Dust and gas are considered as two continuous fluids. Though the dust is comprised of individual grains, and their individual properties are important, the dust is treated as a continuum because the length scales of interest are far above that of individual grains. The dust behaves as a pressureless fluid suspended within the gas. These fluids interact and exchange momentum through a drag force, which models the coupling between the dust and gas.

In the two-fluid set of equations, the dust and gas are treated as distinct continuous fluids. Each fluid is governed by its own set of equations of motion with additional terms representing the drag force that couples the two components. In contrast, the one-fluid description merges the tightly-coupled dust and gas into a single, unified fluid. This is mathematically the same, but views the combined mixture of gas and dust from a common point of reference.

2.1 The two-fluid method

The equations describing the evolution of gas and dust mixtures, where dust is treated as a pressureless, inviscid fluid in the continuum limit, are given by

$$\frac{\mathrm{d}\rho_{\mathrm{g}}}{\mathrm{d}t} = -\rho_{\mathrm{g}}(\nabla \cdot \mathbf{v}_{\mathrm{g}}), \tag{2.1}$$

$$\frac{\mathrm{d}\rho_{\mathrm{d}}}{\mathrm{d}t} = -\rho_{\mathrm{d}}(\nabla \cdot \mathbf{v}_{\mathrm{d}}), \tag{2.2}$$

$$\frac{\mathrm{d}\mathbf{v}_{\mathrm{g}}}{\mathrm{d}t} = \mathbf{f} + \frac{K}{\rho_{\mathrm{g}}}(\mathbf{v}_{\mathrm{d}} - \mathbf{v}_{\mathrm{g}}) - \frac{\nabla P_{\mathrm{g}}}{\rho_{\mathrm{g}}}, \tag{2.3}$$

$$\frac{\mathrm{d}\mathbf{v}_{\mathrm{d}}}{\mathrm{d}t} = \mathbf{f} - \frac{K}{\rho_{\mathrm{d}}}(\mathbf{v}_{\mathrm{d}} - \mathbf{v}_{\mathrm{g}}), \tag{2.4}$$

$$\frac{\mathrm{d}u}{\mathrm{d}t} = -\frac{P_{\mathrm{g}}}{\rho_{\mathrm{g}}}(\nabla \cdot \mathbf{v}_{\mathrm{g}}) + \frac{K}{\rho_{\mathrm{g}}}(\mathbf{v}_{\mathrm{d}} - \mathbf{v}_{\mathrm{g}})^2, \tag{2.5}$$

where $\mathrm{d}/\mathrm{d}t \equiv \partial/\partial t + \mathbf{v} \cdot \nabla$ is the material (Lagrangian) derivative, the subscripts g and d refer to the gas and dust, respectively, ρ is the density, $\mathbf{v}$ is the velocity, P_{g} is the thermodynamic gas pressure, u is the internal energy, and $\mathbf{f}$ represents accelerations acting on both components, such as gravitational acceleration or turbulent driving. The coefficient K denotes the drag coefficient between the two phases, with dimensions of mass per unit volume per unit time. The gas and dust are coupled through

the drag terms, which exchange momentum and energy between the gas and the dust phases.

2.1.1 Equation of sate

The equation set is closed by an equation of state defining the gas pressure. For an ideal gas, this is given by

$$P_{\rm g} = (\gamma - 1)\rho u, \tag{2.6}$$

where γ is the adiabatic index and the sound speed $c_{\rm s}$ is given by

$$c_{\rm s}^2 = \gamma \frac{P_{\rm g}}{\rho_{\rm g}}. \tag{2.7}$$

The pressure can be related to the gas temperature by using

$$P_{\rm g} = \frac{\rho k_{\rm B} T}{\mu m_{\rm H}} \tag{2.8}$$

giving

$$T = \frac{\mu m_{\rm H}}{k_{\rm B}} c_{\rm s}^2, \tag{2.9}$$

where $k_{\rm B}$ is Boltzmann's constant, μ is the mean molecular weight and $m_{\rm H}$ is the mass of a hydrogen atom.

In this work, we consider cold, dense molecular clouds for which $\gamma = 1$ is a reasonable approximation. In this case, the sound speed is constant, as is the temperature of the cloud. Therefore, the gas pressure is calculated according to

$$P_{\rm g} = c_{\rm s}^2 \rho_{\rm g}, \tag{2.10}$$

which means the pressure is proportional to the density.

2.1.2 Stopping time

The stopping time is a characteristic timescale which represents the time required for the drag to adjust the velocity of a dust grain to match the gas velocity. It can be calculated according to

$$t_{\rm s} = \frac{\rho_{\rm g}\rho_{\rm d}}{K(\rho_{\rm d} + \rho_{\rm g})}. \tag{2.11}$$

In general, the drag coefficient, K, depends on the properties of both the gas and dust. The drag regime is determined by the size of the gas molecules' mean free path, $\lambda_{\rm g}$, in comparison to the dust grain size, $s_{\rm grain}$ (Stepinski and Valageas, 1996). This comparison is quantified using the Knudsen number,

$$K_n = \frac{9\lambda_{\rm g}}{4s_{\rm grain}}. \tag{2.12}$$

For $K_n \geq 1$, the drag coefficient is computed using the generalized formula for Epstein drag from Kwok (1975),

$$K = \rho_{\rm g}\rho_{\rm d}\frac{4}{3}\sqrt{\frac{8\pi}{\gamma}}\frac{s_{\rm grain}^2}{m_{\rm grain}}c_{\rm s}f, \tag{2.13}$$

where

$$m_{\rm grain} \equiv \frac{4}{3}\pi\rho_{\rm grain}s_{\rm grain}^3, \tag{2.14}$$

$\rho_{\rm grain}$ is the intrinsic grain density, and f is a correction factor for supersonic motions (Kwok, 1975), given by

$$f \equiv \sqrt{1 + \frac{9\pi}{128}\frac{\Delta\mathbf{v}^2}{c_{\rm s}^2}}. \tag{2.15}$$

The Epstein regime is appropriate for molecular clouds, where the mean free path of the gas is much larger than the size of the dust grains. Under these circumstances, the stopping time for compact, spherical dust grains is

$$t_{\rm s} = \frac{\rho_{\rm grain} s_{\rm grain}}{\rho c_{\rm s} f} \sqrt{\frac{\pi\gamma}{8}}, \tag{2.16}$$

Assuming that all grains have the same intrinsic density, the larger the grain, the longer the stopping time, and consequently, the smaller grains are the most coupled to the gas. The degree of coupling between the dust and the gas is characterised by the Stokes number, which is defined as

$$\mathrm{St} = \frac{t_{\rm s}}{t_{\rm dyn}}, \tag{2.17}$$

where $t_{\rm dyn}$ is the typical dynamical time of the system. For $\mathrm{St} \ll 1$, the gas and dust are dynamically coupled, which implies $\Delta\mathbf{v} \ll c_{\rm s}$ and $f = 1$.

2.2 The one-fluid method

The gas-dust evolution equations given by Equations (2.1)–(2.5) can be reformulated to represent a single fluid moving with the barycentric velocity,

$$\mathbf{v} \equiv \frac{\rho_{\rm g}\mathbf{v}_{\rm g} + \rho_{\rm d}\mathbf{v}_{\rm d}}{\rho_{\rm g} + \rho_{\rm d}}. \tag{2.18}$$

The differential velocity between the two phases, $\Delta\mathbf{v}$, is defined according to

$$\Delta\mathbf{v} \equiv \mathbf{v}_{\rm d} - \mathbf{v}_{\rm g}. \tag{2.19}$$

In this approach, the total density, $\rho = \rho_g + \rho_d$, the barycentric velocity, the differential velocity, and a prescription for specifying the dust fraction, $\epsilon = \rho_d/\rho$, can be used to provide a mathematically equivalent formulation of Equations (2.1)–(2.5). By using the identities $\mathbf{v}_g = \mathbf{v} - (\rho_d/\rho)\Delta\mathbf{v}$ and $\mathbf{v}_d = \mathbf{v} - (\rho_g/\rho)\Delta\mathbf{v}$, Equations (2.1)–(2.5) become

$$\frac{\mathrm{d}\rho}{\mathrm{d}t} = -\rho(\nabla \cdot \mathbf{v}), \tag{2.20}$$

$$\frac{\mathrm{d}\epsilon}{\mathrm{d}t} = -\frac{1}{\rho}\nabla \cdot [\epsilon(1-\epsilon)\rho\Delta\mathbf{v}], \tag{2.21}$$

$$\frac{\mathrm{d}\mathbf{v}}{\mathrm{d}t} = \mathbf{f} - \frac{\nabla P_g}{\rho} - \frac{1}{\rho}\nabla \cdot [\epsilon(1-\epsilon)\rho\Delta\mathbf{v}\Delta\mathbf{v}], \tag{2.22}$$

$$\frac{\mathrm{d}\Delta\mathbf{v}}{\mathrm{d}t} = -\frac{\Delta\mathbf{v}}{t_s} + \frac{\nabla P_g}{(1-\epsilon)\rho} - (\Delta\mathbf{v} \cdot \nabla)\mathbf{v} + \frac{1}{2}\nabla[(2\epsilon - 1)\Delta\mathbf{v}^2], \tag{2.23}$$

$$\frac{\mathrm{d}u}{\mathrm{d}t} = -\frac{P_g}{(1-\epsilon)\rho}\nabla \cdot (\mathbf{v} - \epsilon\Delta\mathbf{v}) + \epsilon(\Delta\mathbf{v} \cdot \nabla)u + \epsilon\frac{\Delta\mathbf{v}^2}{t_s}. \tag{2.24}$$

The dust-to-gas ratio can be calculated according to $\rho_d/\rho_g = \epsilon/(1-\epsilon)$.

2.2.1 Terminal velocity approximation

The fluid equations in the one-fluid formalism can be simplified when the stopping time t_s is small compared to the typical dynamical time-scale, i.e., when $\mathrm{St} < 1$. In

this regime, the relative velocity between the two phases rapidly approaches zero, that is, the dust begins co-moving with the gas on a shorter timescale than the dynamical time. It is worth noting that this assumption is not a requirement for the one-fluid method but significantly enhances its computational efficiency when St << 1, a condition typically satisfied by the dust sizes found in molecular clouds. By applying this terminal velocity approximation, we can neglect the time dependence of the differential velocity between the gas and dust phases, simplifying Equation (2.23) to

$$\Delta \mathbf{v} = \frac{t_{\rm s}}{1-\epsilon}\frac{\nabla P}{\rho}. \tag{2.25}$$

Using this equation for $\Delta \mathbf{v}$, and neglecting terms of second order in $t_{\rm s}$, Equations (2.20)–(2.24) reduce to

$$\frac{{\rm d}\rho}{{\rm d}t} = -\rho(\nabla \cdot \mathbf{v}), \tag{2.26}$$

$$\frac{{\rm d}\epsilon}{{\rm d}t} = -\frac{1}{\rho}\nabla \cdot (\epsilon t_{\rm s} \nabla P_{\rm g}), \tag{2.27}$$

$$\frac{{\rm d}\mathbf{v}}{{\rm d}t} = \mathbf{f} - \frac{\nabla P_{\rm g}}{\rho}, \tag{2.28}$$

$$\frac{{\rm d}u}{{\rm d}t} = -\frac{P_{\rm g}}{(1-\epsilon)\rho}\nabla \cdot \mathbf{v}, \tag{2.29}$$

The equations in the terminal velocity approximation have a strong similarity to the usual hydrodynamic equations, apart from the additional evolution equation for the dust fraction (Equation 2.27).

Chapter 3

Numerical method

We use the Phantom smoothed particle hydrodynamics (SPH) code (Price et al., 2018). Phantom contains numerical methods to solve the gas-dust equations in both the two-fluid and one-fluid prescriptions. Both methods include the back-reaction of the dust on the gas.

3.1 Smoothed particle hydrodynamics

Smoothed Particle Hydrodynamics (SPH) is a computational technique originally designed for astrophysical applications. SPH is a mesh-free, Lagrangian approach, meaning that the computational points (particles) move along with the fluid flow, allowing the coordinates to change dynamically with the system's motion. Over the years, SPH has been extended to a wide range of fields, including fluid dynamics, solid mechanics, and geophysical simulations, due to its flexibility in handling complex

boundary conditions and large deformations. One of its key strengths is the ability to adapt resolution based on local physical properties, like density. This flexibility ensures computational efficiency, as it allocates more particles to regions with higher density or where finer detail is needed, while using fewer particles in less critical areas.

The method works by discretizing the fluid into a set of particles with fixed mass m, which move according to the local fluid velocity $\mathbf{v}$, effectively solving the hydrodynamics equations as the particles flow through the medium. The two fundamental equations representing the position and the conservation of mass in the Lagrangian time derivative form $\mathrm{d}/\mathrm{d}t \equiv \partial/\partial t + \mathbf{v} \cdot \nabla$, are

$$\frac{\mathrm{d}\mathbf{r}}{\mathrm{d}t} = \mathbf{v}, \tag{3.1}$$

$$\frac{\mathrm{d}\rho}{\mathrm{d}t} = -\rho(\nabla \cdot \mathbf{v}), \tag{3.2}$$

where $\mathbf{r}$ is the particle position and ρ is the density.

3.1.1 Interpolation in SPH

In SPH, the density is calculated using a weighted summation over nearby particles, as given by

$$\rho_a = \sum_b m_b W(|\mathbf{r_a} - \mathbf{r_b}|, h_a), \tag{3.3}$$

where a and b are particle labels, m is the mass of the particle, W is the smoothing kernel and h is the smoothing length, determining the rate of fall-off W as a function

of particle spacing. The summation is over neighboring particles, defined as those within $R_{\rm kern}h$, where $R_{\rm kern}$ is the dimensionless cutoff radius of the smoothing kernel. Taking the Lagrangian time derivative of (3.3), one obtains the discrete form of (3.2) in SPH

$$\frac{\mathrm{d}\rho_a}{\mathrm{d}t} = \frac{1}{\Omega_a}\sum_b m_b(\mathbf{v}_a - \mathbf{v}_b)\cdot\nabla_a W_{ab}(h_a) \tag{3.4}$$

where $W_{ab}(h_a) \equiv W(|\mathbf{r_a} - \mathbf{r_b}|, h_a)$, ∇_a denotes the gradient of W taken with respect to the coordinates of particle a keeping h constant, and Ω_a is a term related to the gradient of the smoothing length given by

$$\Omega_a \equiv 1 - \frac{\partial h_a}{\partial \rho_a}\sum_c m_c \frac{\partial W_{ac}(h_a)}{\partial h_a}. \tag{3.5}$$

In Phantom, Equation (3.4) is used to predict the smoothing length at the next time step. Since (3.3), (3.4) and (3.5) all depend on the kernel evaluated on neighbours within R_{kern} times h_a, all three of these summations may be computed simultaneously using a single loop over the same set of neighbours.

In general, a physical quantity A at a particle position a is interpolated by using

$$A_a = \sum_b A_b \frac{m_b}{\rho_b} W(|\mathbf{r_a} - \mathbf{r_b}|, h_a). \tag{3.6}$$

3.1.2 Smoothing kernels

The kernel (weight) function as a function of the smoothing length h and the dimensionless variable $q = |\mathbf{r} - \mathbf{r}'|/h$ can be written in the form

$$W_{ab}(h_a) \equiv \frac{\sigma}{h_a^3} f(q_{ab}), \tag{3.7}$$

where σ is a normalisation constant, and the factor of h_a^3 gives the dimensions of inverse volume. The kernel gradient becomes

$$\nabla_a W_{ab} = \hat{\mathbf{r}}_{ab} F_{ab}, \text{ where } F_{ab} \equiv \frac{\sigma}{h^4} f'(q), \tag{3.8}$$

and the derivative of the kernel with respect to h is

$$\frac{\partial W_{ab}(r,h)}{\partial h} = -\frac{\sigma}{h^4}[3f(q) + qf'(q)]. \tag{3.9}$$

These equations are used in discretising equations of motion in SPH.

In this work, we use the M_4 cubic spline given by

$$f(q) = \begin{cases} 1 - \frac{3}{2}q^2 + \frac{3}{4}q^3, & 0 \le q < 1; \\ \frac{1}{4}(2-q)^3, & 1 \le q < 2; \\ 0 & q \ge 2. \end{cases} \tag{3.10}$$

The cubic spline has a normalization constant $\sigma = 1/\pi$ in 3 dimensions. The discrete form of the continuum normalisation condition, $\int W \mathrm{d}V = 1$, becomes

$$\sum_b \frac{m_b}{\rho_b} W_{ab} \approx 1. \tag{3.11}$$

In general most bell-shaped (Gaussian-like) kernels, such as the cubic spline, fulfill this criterion.

The smoothing length of a particle is given by

$$h_a = 1.2 \left(\frac{m_a}{\rho_a} \right)^{1/3}, \tag{3.12}$$

where the factor 1.2 is an appropriate choice for the cubic spline (Dehnen and Aly, 2012).

A "double hump" kernel (Laibe and Price, 2012) is used to calculate the drag terms in the two-fluid SPH implementation, defining

$$D_{ab}(h_a) = \frac{\sigma}{h_a^3} q_{ab}^2 f(q_{ab}). \tag{3.13}$$

The double hump kernels were found to reduce errors in the calculation of drag forces by a factor of several hundred. This occurs because the kernel is peaked away from the centre, which is beneficial as there is, in general, no contributing particle at the centre. In other words, there is no self-contribution as the drag is between pairs of different types of particles (note that this would be problematic for calculating density as the self-contribution is most important).

3.1.3 Iterations for h and ρ

The mutual dependence of ρ and h means that a root-finding procedure is necessary to solve both (3.3) and (3.12) simultaneously. The procedure implemented in Phantom is solving, for each particle, the equation

$$f(h_a) = \rho_{\rm sum}(h_a) - \rho(h_a) = 0 \tag{3.14}$$

where $\rho_{\rm sum}$ is the density computed from (3.3) and

$$\rho(h_a) = m_a \left(\frac{1.2}{h_a}\right)^3, \tag{3.15}$$

from equation (3.12). Equation (3.14) is solved with Newton-Raphson iterations,

$$h_{a,\rm new} = h_a - \frac{f(h_a)}{f'(h_a)} \tag{3.16}$$

where the derivative is given by

$$f'(h_a) = \sum_b m_b \frac{\partial W_{ab}(h_a)}{\partial h_a} - \frac{\partial \rho_a}{\partial h_a} = -\frac{3\rho_a}{h_a}\Omega_a \tag{3.17}$$

The iterations proceed until $|h_{a,\mathrm{new}} - h_a|/h_{a,0} < \epsilon_h$, where $h_{a,0}$ is the smoothing length of particle a at the start of the iteration procedure and ϵ_h is the tolerance. The convergence with Newton-Raphson is fast, and further iterations are avoided by predicting the smoothing length from the previous timestep according to

$$h_a^0 = h_a + \Delta t \frac{\mathrm{d}h_a}{\mathrm{d}t} = h_a + \Delta t \frac{\partial h_a}{\partial \rho_a}\frac{\mathrm{d}\rho_a}{\mathrm{d}t} \tag{3.18}$$

where $\mathrm{d}\rho_a/\mathrm{d}t$ is evaluated from Equation (3.4).

Since h and ρ are mutually dependent, the code stores only the smoothing length, from which the density can be obtained at any time.

3.1.4 Timestep constraint

The timestep is constrained to be less than the maximum stable timestep according to the Courant condition. For a given particle, a, this is given by

$$\Delta t^a_{\mathrm{cour}} \equiv C_{\mathrm{cour}} \frac{h_a}{c_{\mathrm{s}}} \tag{3.19}$$

where $C_{\mathrm{cour}} = 0.3$ by default (Lattanzio et al., 1984). The resulting timestep is the minimum over all particles:

$$\Delta t = \min_a(\Delta t_a) \tag{3.20}$$

3.2 The two-fluid method in Phantom

In the two-fluid method, the mixture is discretized into two distinct sets of dust and gas particles. Equations (2.1)–(2.2) are discretized with a density summation over neighbors of the same type, giving

$$\rho_a = \sum_b m_b W_{ab}(h_a); \qquad h_a = 1.2\left(\frac{m_a}{\rho_a}\right)^{1/3} \tag{3.21}$$

for the density of a gas particle, and

$$\rho_i = \sum_j m_j W_{ij}(h_i); \qquad h_i = 1.2\left(\frac{m_i}{\rho_i}\right)^{1/3} \tag{3.22}$$

for the density of a dust particle. The indices a and b, refer to quantities computed on gas particles and i and j refer to quantities computed on dust particles.

The discretized equation of motion for the gas particles can be obtained by writing the Lagrangian of the system consisting of gas and dust in SPH and using the Euler-Lagrange equations. Equation (2.3) becomes

$$\frac{\mathrm{d}\mathbf{v}_a}{\mathrm{d}t} = -\sum_b m_b\left[\frac{P_{\mathrm{g},a}}{\Omega_a\rho_a^2}\nabla_a W_{ab}(h_a) + \frac{P_{\mathrm{g},b}}{\Omega_b\rho_b^2}\nabla_a W_{ab}(h_b)\right] - 3\sum_j m_j \frac{\mathbf{v}_{aj}\cdot\hat{\mathbf{r}}_{aj}}{(\rho_a+\rho_j)t_{s,aj}}\hat{\mathbf{r}}_{aj} D_{aj}(h_a), \tag{3.23}$$

where the first summation is the pressure gradient, the second summation is the drag term, Ω_a is a term related to the gradient of the smoothing length

$$\Omega_a \equiv 1 - \frac{\partial h_a}{\partial \rho_a}\sum_b m_b \frac{\partial W_{ab}(h_a)}{\partial h_a}, \tag{3.24}$$

and D is a double hump kernel (Section 3.1.2).

Equation (2.4), the equation of motion for dust particles, is discretized according to

$$\frac{\mathrm{d}\mathbf{v}_i}{\mathrm{d}t} = -3\sum_b m_b \frac{\mathbf{v}_{ib}\cdot\hat{\mathbf{r}}_{ib}}{(\rho_i+\rho_b)t_{\mathrm{s},ib}}\hat{\mathbf{r}}_{ib}D_{ib}(h_b). \tag{3.25}$$

The internal energy equation (Equation 2.5) is discretized as

$$\frac{\mathrm{d}u_a}{\mathrm{d}t} = \frac{P_{\mathrm{g},a}}{\rho_a^2\Omega_a}\sum_b m_b\mathbf{v}_{ab}\cdot\nabla_a W_{ab}(h_a) + 3\sum_j m_j \frac{(\mathbf{v}_{aj}\cdot\hat{\mathbf{r}}_{aj})^2}{(\rho_a+\rho_j)t_{\mathrm{s},aj}}\, D_{aj}(h_a), \tag{3.26}$$

where the two terms are from pressure and drag heating, respectively.

The stopping time, $t_{\mathrm{s},ai}$, is defined between a pair of gas and dust particles, given by

$$t_{\mathrm{s},ai} = \frac{\rho_a\rho_i}{K_{ai}(\rho_a+\rho_i)}, \tag{3.27}$$

where a refers to a gas particle and i a dust particle.

In the two-fluid method, the timestep is also constrained by the stopping time according to

$$\Delta t^a_{\mathrm{drag}} = \min_j(t_{\mathrm{s},aj}). \tag{3.28}$$

Laibe and Price (2012) demonstrate the two-fluid method also has a spatial resolution requirement in order to correctly predict the dust dynamics. This is given by

$$h \lesssim c_{\mathrm{s}}t_{\mathrm{s}}. \tag{3.29}$$

The combination of the drag timestep criterion and spatial resolution requirement mean that these can become prohibitively expensive when the drag is large. That is, when $\mathrm{St} < 1$, which typically occurs for small dust grains.

3.3 The one-fluid method in Phantom

In the one-fluid method, only one set of particles is used to represent the mixture of gas and dust. Discretizing Equations (2.26), (2.28), and (2.29) is straightforward as there is only one type of particle with no drag terms. Equation (2.26) for the total density becomes

$$\rho_a = \sum_b m_b W_{ab}(h_a); \qquad h_a = 1.2\left(\frac{m_a}{\rho_a}\right)^{1/3}. \tag{3.30}$$

Equation (2.28) is discretized as

$$\frac{\mathrm{d}\mathbf{v}_a}{\mathrm{d}t} = -\sum_b m_b \left[\frac{P_{\mathrm{g},a}}{\Omega_a \rho_a^2}\nabla_a W_{ab}(h_a) + \frac{P_{\mathrm{g},b}}{\Omega_b \rho_b^2}\nabla_a W_{ab}(h_b)\right], \tag{3.31}$$

and Equation (2.29) becomes

$$\frac{\mathrm{d}u_a}{\mathrm{d}t} = \frac{P_{\mathrm{g},a}}{\rho_a^2 \Omega_a}\sum_b m_b \mathbf{v}_{ab}\cdot\nabla_a W_{ab}(h_a). \tag{3.32}$$

Discretizing Equation (2.27) does not place any constraint that the dust fraction should be between $0 \leq \epsilon \leq 1$. Mapping the dust fraction to a function whose co-domain is only defined from $[0, 1]$ can prevent ϵ from becoming unphysical. Ballabio et al. (2018) suggest a parameterization that meets this criterion, given by

$$\epsilon = \frac{s^2}{1+s^2}, \tag{3.33}$$

such that

$$s = \sqrt{\frac{\epsilon}{1-\epsilon}}. \tag{3.34}$$

In this formulation, s is then related simply to the ratio of dust to gas densities,

$s = \sqrt{\rho_{\rm d}/\rho_{\rm g}}$. By substituting the time derivative of the new parameter,

$$\frac{{\rm d}s}{{\rm d}t} = \frac{1}{2s(1-\epsilon)^2}\frac{{\rm d}\epsilon}{{\rm d}t}, \tag{3.35}$$

in Equation (2.27), the following can be obtained,

$$\frac{{\rm d}s}{{\rm d}t} = -\frac{1}{2\rho(1-\epsilon)^2}\left\{\nabla\cdot\left[s(1-\epsilon)t_{\rm s}\nabla P_{\rm g}\right] + (1-\epsilon)t_{\rm s}\nabla P_{\rm g}\cdot\nabla s\right\}. \tag{3.36}$$

The SPH discretization is implemented in the form

$$\frac{{\rm d}s_a}{{\rm d}t} = -\frac{1}{2\rho_a(1-\epsilon_a)^2}\sum_b\left[\frac{m_b s_b}{\rho_b}(D_a + D_b)(P_a - P_b)\frac{\bar{F}_{ab}}{|r_{ab}|}\right], \tag{3.37}$$

where $D_a = t_{{\rm s},a}(1-\epsilon_a)$, $\bar{F}_{ab} = [F_{ab}(h_a) + F_{ab}(h_b)]/2$, and $F_{ab} \equiv (\sigma/h^4)f'(q)$. This equation conserves linear and angular momentum, energy, and mass – at least up to the accuracy of the time stepping algorithm.

In addition, the diffusion equation for the dust fraction (Equation (2.27)), which models the distribution of dust in the gas fluid, imposes an additional constraint on the timestep in addition to the Courant timestep (Price and Laibe, 2015). This timestep criterion is given by

$$\Delta t < \Delta t_\epsilon \equiv C_0\frac{h^2}{\epsilon t_{\rm s} c_{\rm s}^2}, \tag{3.38}$$

where C_0 is a dimensionless safety factor of order unity. Note that this timestep criterion is inversely proportional to the stopping time, which is opposite the timestep criterion for the two-fluid method (via Equation (3.28)). Thus, the timestep becomes limiting as the stopping time becomes large, occurring when dust grains are large. Ballabio et al. (2018) derive a general form of the timestep criterion accounting for

gradients in ϵ. As with their recommendation, we use the simpler criterion given by Equation (3.38) since it avoids calculating these ϵ gradients.

3.3.1 Limiting the stopping time

As mentioned in Section 2.2.1, the one-fluid method relies on the terminal velocity approximation. This remains accurate when $\mathrm{St} \leq 1$, a condition typically met by small dust grains. However, when $\mathrm{St} > 1$, inaccuracies due to assumption violations can arise. Notably, for medium-sized particles even with initial Stokes numbers slightly below one, the Stokes number can increase beyond one over time, leading to a breakdown of the approximation.

Ballabio et al. (2018) suggest limiting the stopping time on particles where $\mathrm{St} > 1$, replacing the stopping time (t_s) by the limited stopping time ($\tilde{t}_\mathrm{s}$), given by

$$\tilde{t}_\mathrm{s} = \min(t_\mathrm{s}, h/c_\mathrm{s}). \tag{3.39}$$

This restricts changes in the dust fraction for particles that do not adhere to the terminal velocity approximation, curbing potential errors in dust mass conservation.

Another way to view the limiter is that there is a spatial resolution requirement for the one-fluid method that is analogous to the resolution requirement for the two-fluid method (Equation 3.29). That is,

$$h \gtrsim c_\mathrm{s} t_\mathrm{s}. \tag{3.40}$$

The smoothing length must be larger than the coupling scale of gas and dust. For the two-fluid method, the resolution must be sufficient to resolve the length scale

over which gas and dust would begin co-moving. For the one-fluid method, the terminal velocity approximation assumes that the gas and dust are co-moving below the resolution scale. Violation of this assumption is problematic because it introduces errors that dominate the physical solution.

3.4 Stokes numbers in SPH

The Stokes number is defined as the ratio of stopping time to dynamical time (Equation (2.17)). It is a dimensionless quantity that measures the degree of coupling between the gas and dust. We calculate the Stokes number per particle defined in terms of the local dynamical time, $t_{\rm dyn} = h/c_{\rm s}$. It would seem sensible to use the characteristic timescale of the turbulence, $t_{\rm c} = L/2\mathcal{M}c_{\rm s}$, as the dynamical time, but the local dynamical time is more important in terms of the numerics of the algorithms, as will be shown.

Defining the Stokes number in terms of the local dynamical time introduces a resolution dependence because the dynamical time is proportional to h. This means that the Stokes number increases as h decreases, even if the density and dust grain properties are held constant. Therefore, even if the terminal velocity approximation in the one-fluid method is valid at one resolution, there is always a larger resolution for which this will no longer be true (see discussion on the one-fluid limiter in Section 3.3.1).

For the two-fluid method, the problem is reversed. The Stokes number goes down

as h increases (i.e., decreasing resolution). This means that there is a point where the spatial resolution requirement is no longer satisfied via Equation (3.29).

Calculating the Stokes number requires the dust stopping time. For the one-fluid method, this is calculated using Equation (2.16). Each particle carries the total density (gas plus dust density), so it is trivial to calculate. Note that the one-fluid method does not apply the supersonic correction given by Equation (2.15).

The Stokes number for the two-fluid method is less straightforward because the stopping time is calculated per gas-dust particle pair (Equation (3.27)). Each dust particle has a stopping time with each gas particle it interacts with. We desire a single Stokes number per dust particle. To estimate a single stopping time for dust particles, the gas density is interpolated at the location of the dust particle, and the combined dust plus interpolated gas density is used to calculate a single stopping time per dust particle. The gas velocity is also interpolated at the location of the dust so that the supersonic correction term can be calculated, which requires the differential velocity between the gas and dust.

Chapter 4

Simulation Conditions and Results

4.1 Simulation conditions

We conduct experiments of driven, isothermal, supersonic turbulence in a periodic box. We have chosen initial conditions that represents the interior of molecular clouds specifically corresponds to Stokes numbers around one to explore the properties of the numerical methods. Simulations are performed using the one-fluid and two-fluid methods for dust grains of size 3 μm and 10 μm. The intrinsic density of dust grains is 3 g cm^{-3}, representing a combination of carbonaceous (2.2 g cm^{-3}) and silicate grains (3.5 g cm^{-3}). The box size is x, y, $z \in [0, L]$ with $L = 3$ pc per side. The initial density is uniform with a mean total density (gas plus dust) of $\rho_0 = 10^{-20}$g cm^{-3}. This corresponds to a number density of $n \sim 2.6 \times 10^3$ cm^{-3} for a mean molecular weight of 2.3. We use an isothermal equation of state ($\gamma = 1$) with a sound speed $c_s = 0.2$

km s^{-1}, corresponding to a temperature of $T \approx 11.5$ K. The equation of state is well represented by an isothermal equation of state for these densities (Scalo et al., 1998; Bergin and Tafalla, 2007). Simulations are performed using 256^3 particles.

The turbulence is driven to keep a root-mean squared (rms) velocity of Mach 10 ($\mathcal{M}$ = 10). The simulation is performed for 12 turbulent crossing times, defined as $t_c = L/2\mathcal{M}c_s \approx 0.733$ M yr. The driving pattern uses a force derived from an Ornstein-Uhlehnbeck process (Eswaran and Pope, 1988; Schmidt et al., 2009; Federrath et al., 2010). This is an idealized model that represents the physical processes that generate the turbulence. The generate turbulence, like supernovae. The autocorrelation timescale of the driving is 1 t_c, meaning that statistically independent snapshots are produced every turbulent crossover time. The driving is purely solenoidal. All calculations utilize the same driving pattern.

By using the Stokes number definition (Equation 2.17), with $t_{dyn} = h/c_s$, Equation (3.12), and the mass per particle defined as $m_a = \rho_0 L^3/n$, where n_{SPH} is the number of SPH particles, an equation for the initial Stokes number of our turbulence inside a periodic box setup can be obtained as

$$\mathrm{St} = 0.04332 \left(\frac{\rho_{grain}}{3\,\mathrm{g\ cm^{-3}}}\right)\left(\frac{s_{grain}}{0.1\,\mu\mathrm{m}}\right)\left(\frac{n_{SPH}}{256^3}\right)^{1/3}\left(\frac{\rho_a}{10^{-20}\,\mathrm{g\ cm^{-3}}}\right)^{-1}\left(\frac{L}{3\,\mathrm{pc}}\right)^{-1}. \quad (4.1)$$

The conditions in Equation (4.1) reflect typical dust grain sizes and conditions for molecular clouds. Note that this equation assumes that there is no initial velocity, and that the initial density is uniform, as is the case for our initial conditions. The Stokes number will change per particle as turbulence develops.

Via Equation (4.1), dust grains with sizes 3 and 10 μm in these initial conditions correspond to initial Stokes numbers of St = 1.3 and St = 4.3, respectively. These Stokes number regimes are specifically chosen to avoid excessively high resolution requirements for the two-fluid method (via Equation 3.29). For density variations of 100× increase and decrease around the mean density, which can be expected for isothermal, supersonic turbulence, this implies Stokes number variations of approximately 20×. For the one-fluid method, it is thus expected that the terminal velocity approximation will be reasonably upheld for a significant fraction of particles.

4.2 Results

Our analysis focuses on the time-averaged statistical properties of turbulent dust and gas. The initial turbulent crossing from t/t_c = 0 to t/t_c = 2 is excluded from our analysis as the turbulence is not fully developed during this phase. We perform averaging over 11 snapshots in the range t/t_c = 2–12, each taken 1 t_c apart such that they are statistically independent snapshots.

4.2.1 Gas density

Figure (4.1) shows column-integrated gas densities at $t/t_c = 2, 3, 4, 5$ for 3 μm and 10 μm dust grains using the two-fluid and one-fluid methods. At t/t_c = 2, the gas column densities in both methods are comparable. However, they diverge over time. While they still show the same large-scale structure, different structures appear on smaller

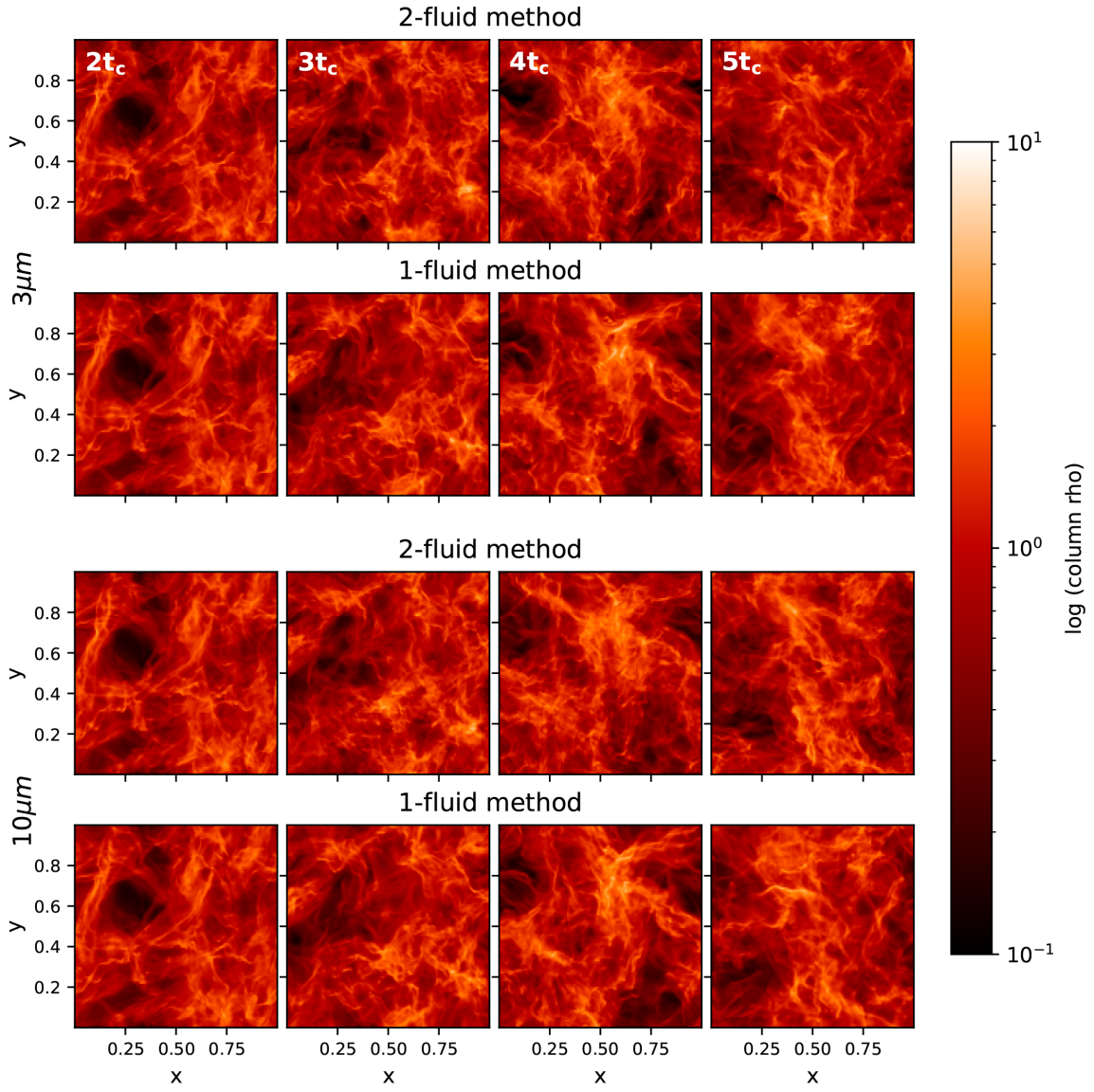

Figure 4.1: Column density of the gas with 3 μm dust grains (top panel) and 10 μm dust grains (bottom panel) in the two-fluid method (top row of each panel) and in the one-fluid method (bottom row of each panel) at $t/t_c = 2, 3, 4, 5$ from left to right columns, respectively.

scales. Though all calculations use the same driving pattern, the chaotic nature of the turbulence means that individual realizations of the density field will be different across each calculation.

Figure (4.2) shows the time-averaged, volume-weighted probability density functions (PDFs) of the gas density for 3 μm and 10 μm dust grains. The volume-weighted PDFs are calculated by interpolating the particle densities for each turbulent turnover snapshot onto a grid with a resolution of 512^3 cells, i.e., twice the number of particles. The PDFs are not calculated using the particles directly because this would lead to a mass-weighted PDF. Time averaging helps to mitigate the effects of turbulent variability and is necessary to ensure statistically meaningful results.

The gas PDFs exhibit a log-normal distribution, characteristic of supersonic, isothermal turbulence (e.g., Vazquez-Semadeni, 1994; Passot and Vázquez-Semadeni, 1998). They can be fit in log-space to a normal distribution with Table 4.1 giving the mean and standard deviation of each fit. No significant difference in the gas PDFs are found between the simulations with 3 μm and 10 μm dust grains, or between the two-fluid and one-fluid methods.

Table 4.1: Log-normal fits of the gas density PDFs

Size (s)	Method	Mean	Std dev (σ)
3 μm	Two-fluid	-1.2972 ± 0.0055	1.5930 ± 0.0055
3 μm	One-fluid	-1.2638 ± 0.0051	1.5580 ± 0.0051
10 μm	Two-fluid	-1.2748 ± 0.0056	1.5750 ± 0.0056

Table 4.1: (Continued) Log-normal fits of the gas density PDFs

Size (s)	Method	Mean	Std dev (σ)
10 μm	One-fluid	-1.2839 ± 0.0053	1.5779 ± 0.0053

4.2.2 Dust density

Figure (4.3) shows the column-integrated dust density at $t/t_{\rm c}$ = 2, 3, 4, 5 for 3 μm and 10 μm dust grains in the two-fluid and one-fluid methods, similar to the gas density renderings in Figure (4.1). The dust density fields are almost exactly the same between the two-fluid and one-fluid for both grain sizes at $t/t_{\rm c}$ = 2. The density fields diverge over time. The large-scale structures remain similar at t/t_c = 5, but small-scale differences are evident. This behaviour was also seen in the column-integrated gas density.

Figure (4.4) shows the PDFs of dust density for 3 μm and 10 μm dust grains. The PDFs for both grain sizes peak at similar values. The peaks are located at lower densities than the gas PDFs, shifted an amount appropriate for the mean dust-to-gas ratio. For both grain sizes, the high-density tails of the dust PDFs are closely aligned for both methods, though the two-fluid tail extends to slightly higher densities. The largest difference is in the low-end tail. The two-fluid results extend several orders of magnitude lower than the one-fluid results. The implication of this is that the two-fluid dust density PDFs are more asymmetric than the one-fluid PDFs.

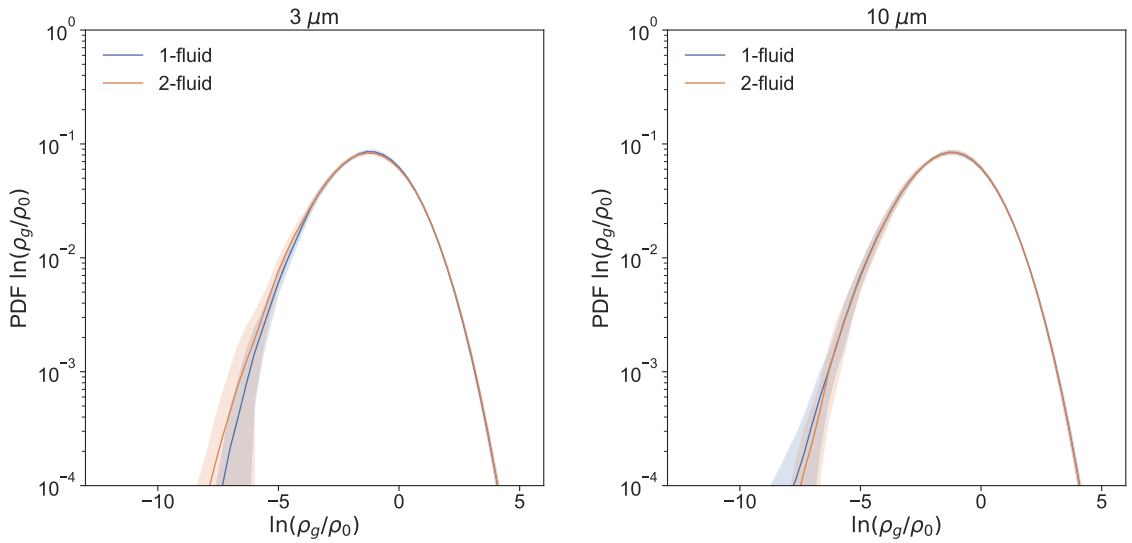

Figure 4.2: Time-averaged volume weighted PDFs of $\ln(\rho_{\rm g}/\rho_0)$ for $3\,\mu$m (left) and $10\,\mu$m (right) in 256^3 resolution in one-fluid and two-fluid methods. Shaded regions represent the standard deviation of the time averaging.

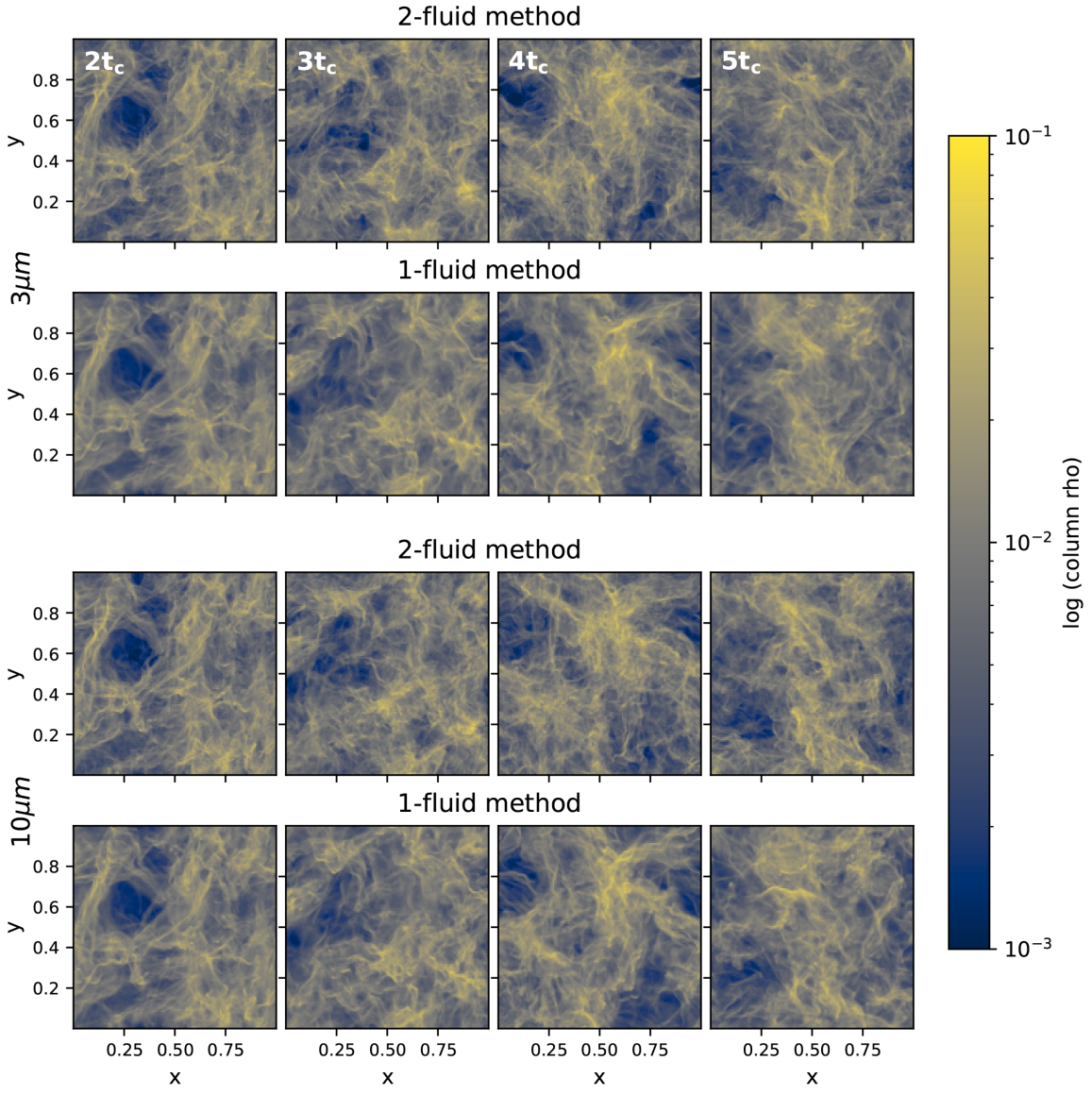

Figure 4.3: Column density of the 3 and 10 μm dust in the two-fluid and one-fluid methods at $t/t_c = 2, 3, 4, 5$ (left to right columns, respectively).

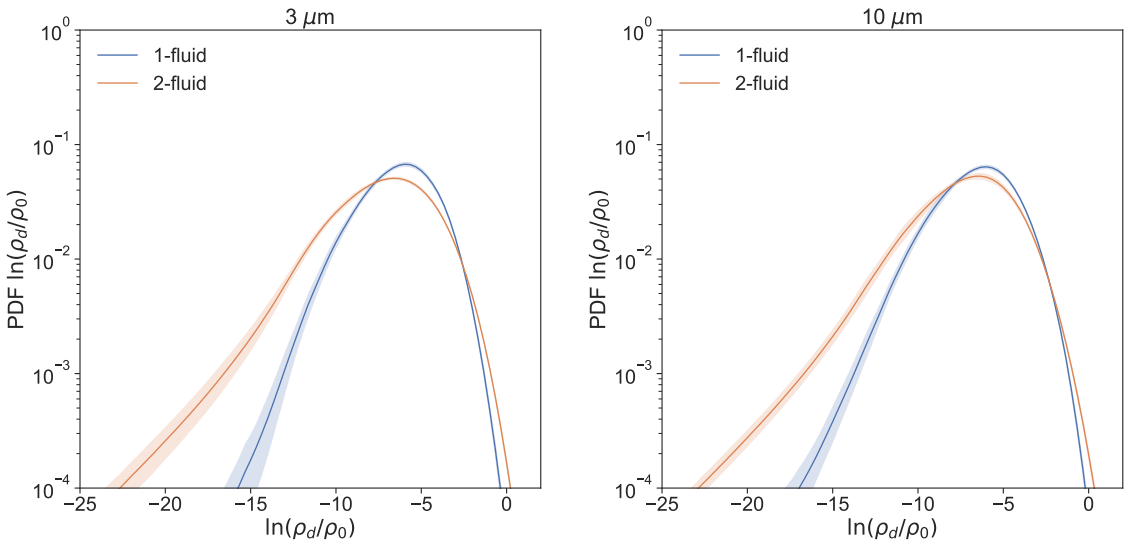

Figure 4.4: Time-averaged volume-weighted PDFs of $\ln(\rho_{\rm d}/\rho_0)$ for 3 mum (left) and 10 μm (right) in 256^3 resolution in one-fluid and two-fluid methods. Shaded regions represent the standard deviation of the time averaging.

Table 4.2: Log-normal fits of the dust density PDFs

Size (s)	Method	Mean	Std dev (σ)
3 μm	Two-fluid	-6.9776 ± 0.0270	2.5923 ± 0.0270
3 μm	One-fluid	-6.1704 ± 0.0190	1.9784 ± 0.0190
10 μm	Two-fluid	-6.8726 ± 0.0296	2.4853 ± 0.0296
10 μm	One-fluid	-6.3531 ± 0.0205	2.0863 ± 0.0205

Table (4.2) lists the mean and standard deviations for the dust density PDFs fit to log-normal distributions. The fitted parameters are consistent for the same method, although they are different between the one-fluid and two-fluid methods. The mean values are lower for the two-fluid fits compared to the one-fluid fits, along with a wider standard deviation. Overall, the dust density PDFs have larger standard deviations than the gas density PDFs, in addition to larger errors on the fitted parameters. This means that the dust density PDFs deviate in shape from the gas density PDFs, which can also be understood as a consequence of the asymmetries in the dust density PDFs found in Figure (4.4).

4.2.3 Correlation of dust and gas

Figure (4.5) compares the column densities of the gas (top row) and dust (bottom row) for 3 μm (left panel) and 10 μm (right panel) dust grains in the two-fluid method (left column of each panel) and the one-fluid method (right column of each panel)

at $t/t_c = 5$. The large-scale structure of the dust follows the gas in both methods for both grain sizes. However, the dust column density in the two-fluid method appears to exhibit sharper density contrasts on the small scale compared to the gas density. The one-fluid dust density also has sharper density contrasts than the gas, but not as pronounced as the two-fluid dust density.

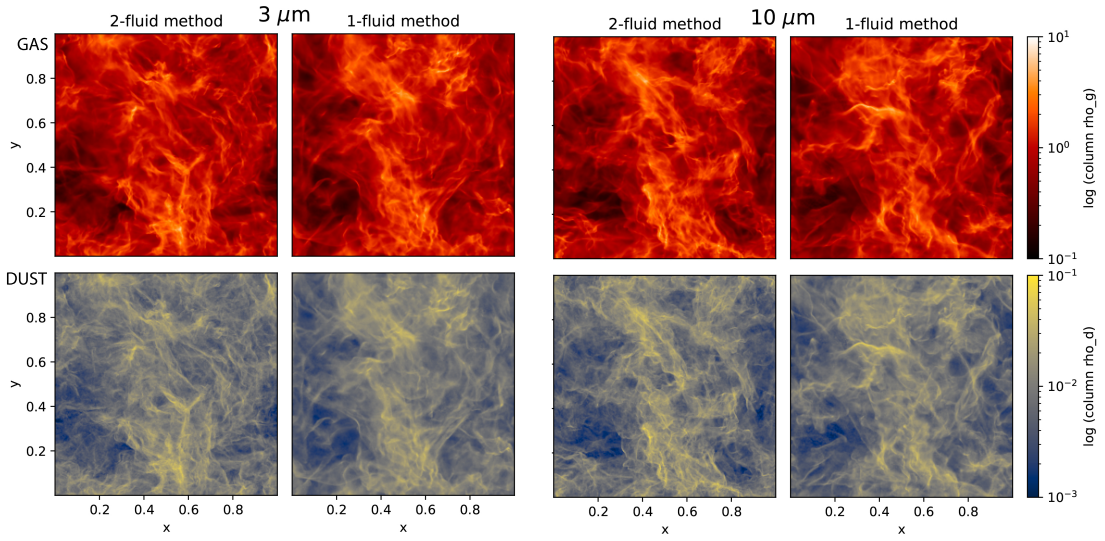

Figure 4.5: Column density of the gas (top row) and the dust (bottom row) for 3 μm and 10 μm dust grains (left and right panels, respectively) in the two-fluid method (left column of each panel) and the one-fluid method (right column of each panel) at $t/t_c = 2$ (≈ 1.47 Myr).

Figure (4.6) shows slices of the dust and gas densities at $t/t_c = 5$ for 3 μm and 10 μm dust grains in the two-fluid and one-fluid methods. A similar picture emerges as with the column-integrated densities, but even more pronounced. The large-scale

structure of the dust traces the structure of the gas, however the density contrast between low- and high-density regions in the dust are greater than the gas. This appears more pronounced for the two-fluid method than the one-fluid method, suggesting that decoupling occurs more readily for the two-fluid method.

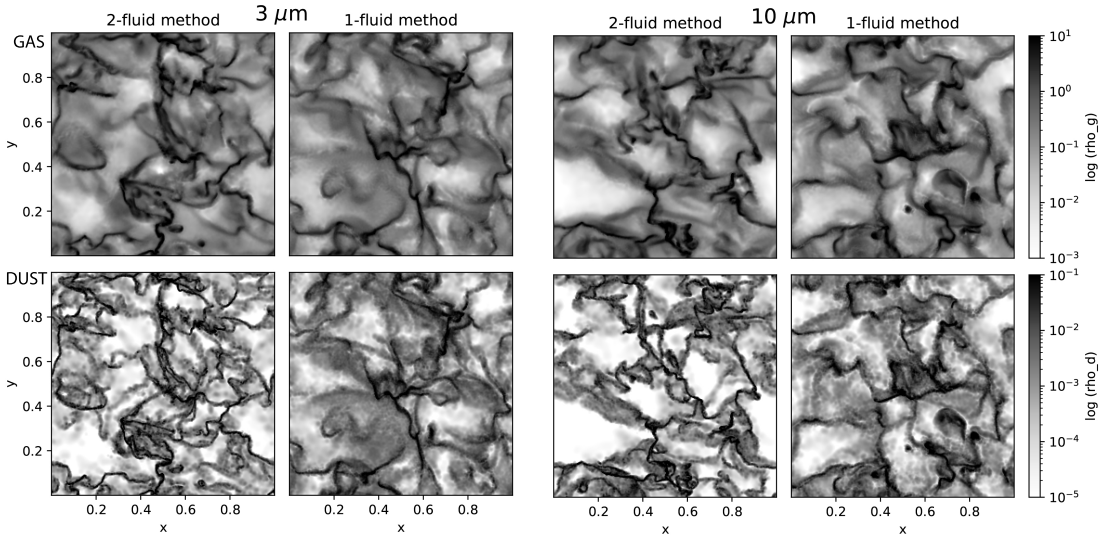

Figure 4.6: Slices of the gas (top row) and the dust (bottom row) densities for 3μm and 10 μm dust grains (left and right panels, respectively) in the two-fluid method (left column of each panel) and the one-fluid method (right column of each panel) at $t/t_c = 5$ (≈ 3.67 Myr).

Figure (4.7) depicts the probability density functions (PDFs) of dust-to-gas ratio for dust grains of sizes 3 μm and 10 μm. They both peak at approximately the mean dust-to-gas ratio of 0.01. The PDFs for the two-fluid dust-to-gas ratios are significantly broader than the PDFs obtained using the one-fluid method. Both PDFs

are asymmetric, though the two-fluid has a larger skew.

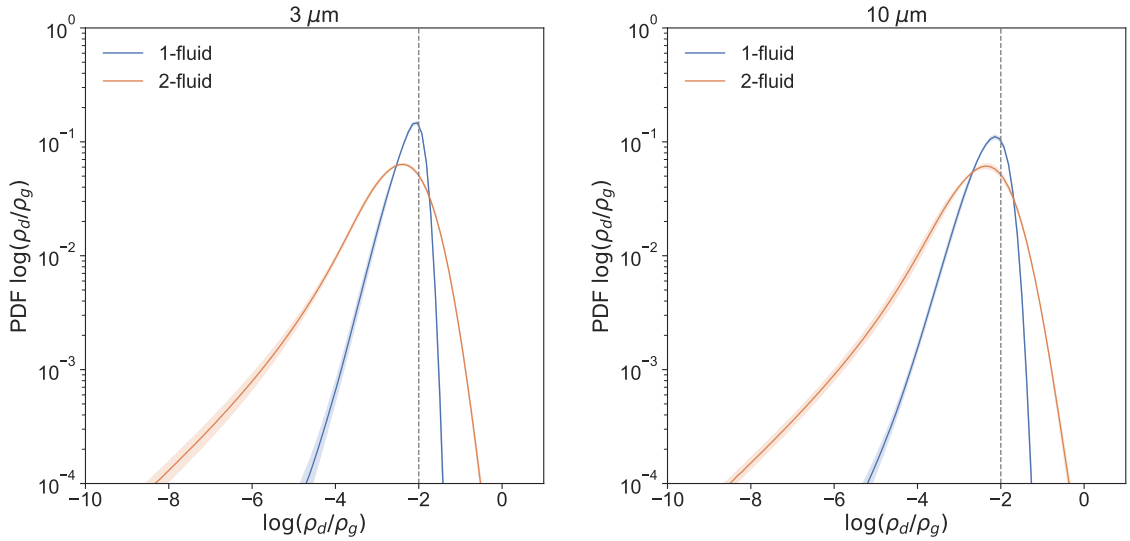

Figure 4.7: Time-averaged volume-weighted PDFs of $\log(\rho_{\rm d}/\rho_{\rm g})$ for 3 μm (left) and 10 μm (right) in 256^3 resolution in the two-fluid and one-fluid approaches. Shaded regions represent the standard deviation of the time averaging.

The one-fluid method reaches a maximum dust-to-gas ratio of ~ 0.03 for 3 μm and ~ 0.05 for 10 μm dust grains, whereas the two-fluid method reaches a maximum dust-to-gas ratio of ~ 0.30 for 3 μm and ~ 0.39 for 10 μm dust grains. This represents a local increase from the mean dust-to-gas ratio of 3–5× with the one-fluid method, but a 30–39× increase with the two-fluid method. This increase requires a corresponding decrease in the minimum dust-to-gas ratios observed in the results. The minimum dust-to-gas ratios in the PDFs are not significantly different between 3 and 10 μm dust grains for the two-fluid method, though the PDFs for the one-fluid are slightly

broader for 10 μm grains compared to 3 μm grains.

That the dust-to-gas ratio distributions are narrower for the one-fluid results than the two-fluid results can be understood in context of the stopping time limiter used with the one-fluid method. The limiter is applied in low-density regions. As seen in Figure (4.6), there is more dust mass in low-density regions for the one-fluid method compared to the two-fluid method. This homogenizes the dust throughout the domain, yielding a narrow distribution of dust-to-gas ratios.

4.2.4 Stokes number

The Stokes number, St = $t_{\rm s}/t_{\rm dyn}$ (Equation 2.17), is a dimensionless quantity that measures the degree of coupling between the gas and dust. We calculate the Stokes number per particle defined in terms of the local dynamical time, $t_{\rm dyn} = h/c_{\rm s}$, as described in Section (3.4).

Figure (4.8) shows the probability distribution of the logarithm of Stokes numbers over the SPH particles at $t/t_{\rm c} = 8$. Naively, one would expect the two-fluid and one-fluid Stokes number distributions to be equal since the simulations have the same grain density, same grain size, same resolution, and gas density distributions (see Section 4.2.1). This is true below St < 1, with the two-fluid and one-fluid results in good agreement for both the 3 and 10 μm dust grain calculations. The Stokes number distributions for 3 μm dust grains peak roughly 3× smaller than the peak for the 10 μm distribution, reflecting the dependence of the Stokes number on grain size (via

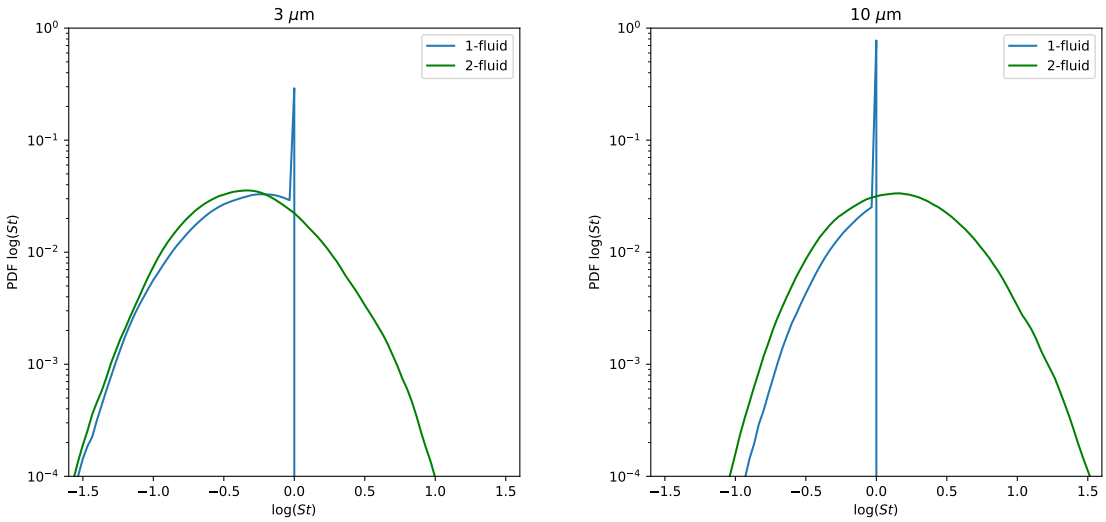

Figure 4.8: PDFs of log(St) for 3 μm (left) and 10 μm (right) in 256^3 resolution in two-fluid and one-fluid approaches at $t/t_c = 8$

the stopping time).

The large spike at St = 1 for the one-fluid results is a consequence of the stopping time limiter (Equation 3.39). The limiter prohibits stopping times greater than the dynamical time because of the terminal velocity approximation, thereby artificially capping the Stokes number at 1. One way to view this is that the dust grains act as though they have smaller size ($s_{\rm grain}$).

Approximately 30% and 75% of the particles are in the St > 1 regime for the 3 and 10 μm dust grain simulations, respectively. Thus, the one-fluid limiter is applied to approximately 30% and 75% of the particles. This results in artificially enhanced coupling. In effect, it is as if the calculations have a population of dust grains from

0.3 to 3 μm or 0.3 to 10 μm, reflecting the maximum Stokes number of the 3 and 10 μm calculations. It is important to note that the limiter is critical for numerical stability in this regime (see Section 4.2.5).

Conversely, even though the stopping time is not limited for the two-fluid results, the numerical resolution requirement (St > 1, see Equation 3.29) implies that this is not upheld for 70% and 25% of particles in the 3 and 10 μm simulations, respectively. This means that the one-fluid results are most accurate for St < 1 and the two-fluid results most accurate for $St > 1$.

The distribution of Stokes numbers can be understood from the dependence on density (and indirectly smoothing length), as all other conditions remain constant. In SPH, the mass of each particle is constant. Thus, the smoothing length can be related to density as $h \propto \rho^{-1/3}$ through Equation (3.12), and the dynamical time expressed in terms of density as $t_{\rm dyn} \propto \rho^{-1/3}$. As the stopping time is proportional to inverse of total density through Equation (2.16), that is, $t_{\rm s} \propto \rho^{-1}$, the Stokes number of a particle therefore scales according to $\mathrm{St} \propto \rho^{-2/3}$.

The expected statistics of the Stokes number distributions can be understood in relation to the gas density PDF. The standard deviation of the two-fluid Stokes number distributions, given in natural logarithm to match the gas density distribution statistics, is 0.87 for 3 μm and 0.89 for 10 μm. The gas density PDFs have standard deviations of approximately 1.56 for all simulations (Table 4.1). This is close to the value expected by the $\mathrm{St} \propto \rho^{-2/3}$ scaling relation, keeping in mind that the Stokes

number distribution is calculated on the particles and the gas density distribution on the interpolated grid.

4.2.5 Impact of the Dust Limiter

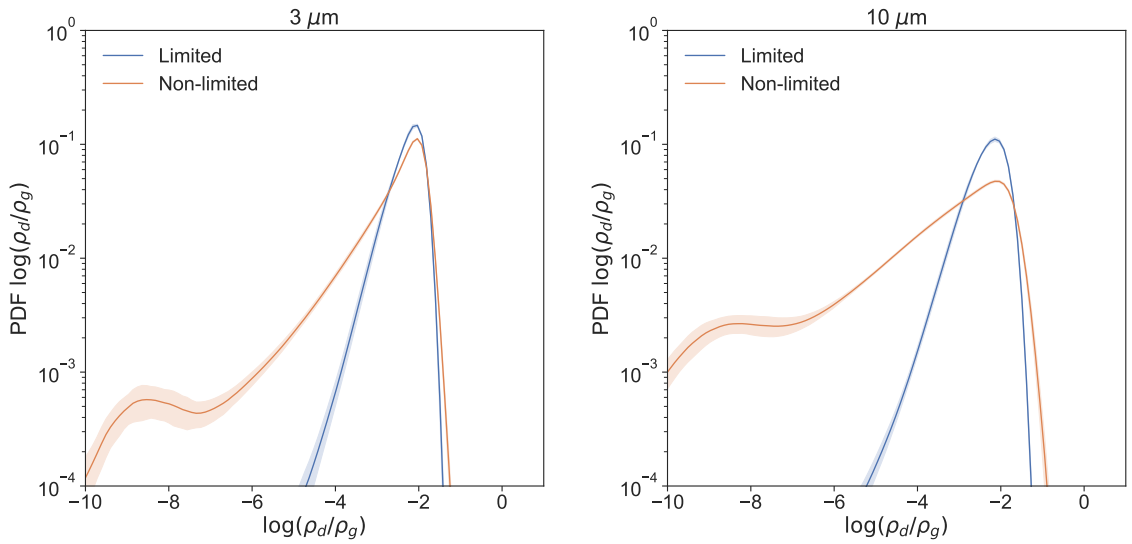

Figure 4.9: Time-averaged volume weighted PDFs of $\log(\rho_d/\rho_g)$ for 1μm (left) and 3μm (right) in 256^3 resolution in the one-fluid and non-limited one-fluid methods. Shaded regions represent the standard deviation of the time averaging.

The one-fluid method uses a limiter on the stopping time when St > 1 in order to maintain the terminal velocity approximation. This artificially keeps the dust in the St ≤ 1 regime, which in effect causes the dust to be more strongly coupled to the gas. Despite this seemingly undesirable behaviour, the stopping time limiter is critical for our calculations since approximately 30% and 75% of particles are in the

St > 1 regime for the 3 and 10 μm grain size simulations, respectively.

Figure (4.9) shows the PDFs of dust-to-gas ratio for one-fluid simulations with and without the stopping time limiter. Without the limiter, a spurious peak appears at very low dust-to-gas ratios. This is entirely numerical in origin. A similar peak can be found in the results of Tricco et al. (2017). This peak disappears when the limiter is used. In fact, the limiter also reduces the range of dust-to-gas ratios, as discussed in Section (4.2.3).

The right-hand tail of the dust-to-gas ratio PDFs are closely aligned between the limited and non-limited results. The limiter is only applied to regions where St > 1, implying that if there is agreement in the larger dust-to-gas ratio regions, then this condition occurs most predominantly inside of dense filaments. The right-hand tails for the limited and non-limited results are in particularly close agreement for the 3 μm simulations, as a greater fraction (approximately 70%) of the particles stay below St = 1.

Figure (4.10) shows the mean dust-to-gas ratio as calculated on the particles for results with and without the limiter. For 3 μm grains, there is a small, but noticeable increase in the mean dust-to-gas ratio from 1.014% with the limiter to 1.024% without at $t/t_c = 12$. However, there is a significantly greater difference between the limited and non-limited results for 10 μm dust grains. With the limiter, the mean dust-to-gas ratio is 1.022% at $t/t_c = 12$. Without the limiter, the mean dust-to-gas ratio steadily increases over time, reaching a mean dust-to-gas ratio of 1.14% before experiencing

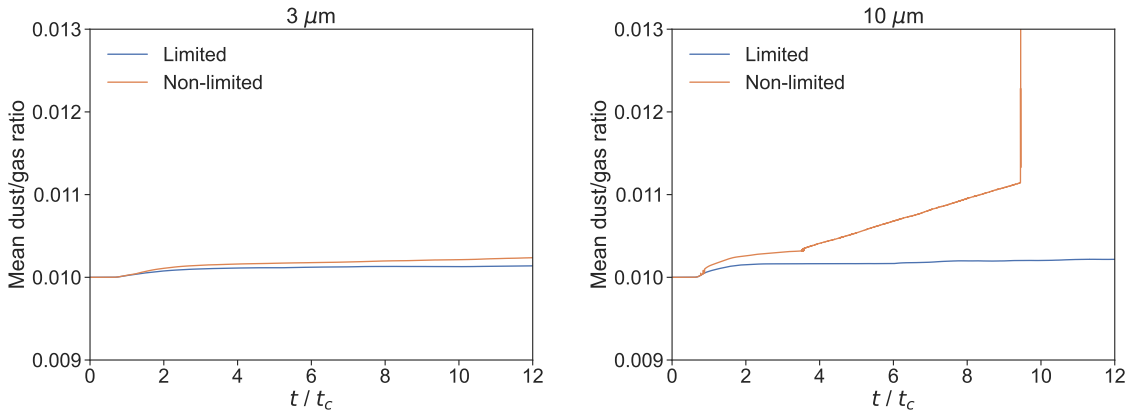

Figure 4.10: Mean dust-to-gas ratio calculated on the particles in the one-fluid method with and without the stopping time limiter for 3μm (left) and 10μm (right) in 256^3 resolution.

numerical instability around $t/t_c \approx 9.5$. This occurs due to the violation of dust mass conservation, in that, dust mass increases over time due to numerical error.

That numerical instability occurs without the limiter is a consequence of the dynamical nature of our dusty turbulence calculations. Low-density particles, that is, particles with St > 1, can experience spurious increase in dust mass. For Ballabio et al. (2018), these errors occur on the periphery of a protoplanetary disc, which has little dynamical impact on the interior of the disc. However, in our calculations, the errors on these low-density particles quickly gets recycled into high-density filaments because the turbulence is driven for multiple turbulent crossing times. These errors compound over time. Though the limiter avoids catastrophic numerical failure, it does introduce some numerical effect on our results. The limiter has the same practical

effect as changing the dust grain size. As an extreme example, a simulation with 1 cm grains should give results equivalent to simulations with 10 cm grains because in both cases all particles would be limited to St = 1.

Chapter 5

Conclusion

We performed simulations of dusty, isothermal turbulence using 3 and 10 μm dust grains in initial conditions representative of cold, dense molecular clouds. Turbulent driving was applied to create and sustain supersonic $\mathcal{M}$ = 10 turbulence over 12 turbulent crossing times.

Simulations were performed using two-fluid and one-fluid methods. Both treat the dust as a continuous, pressureless fluid. For the two-fluid dust method, gas and dust are modelled using distinct sets of particles. These two types of particles are coupled together through a drag term. For the one-fluid method, a single species of particle is used that represent the mixture of gas and dust. Particles exchange dust between them, which changes the dust fraction of each particle. We use the terminal velocity approximation for the one-fluid method, in which case dust evolution acts like a diffusion process. The stopping time limiter of Ballabio et al. (2018) was employed

for numerical stability

The Stokes numbers of the initial conditions for our 256^3 particle resolution calculations were St = 1.3 and St = 4.3 for 3 and 10 μm dust grains, respectively. Note that the Stokes number in our definition uses the local dynamical time, which is the most relevant timescale for the numerical methods. This Stokes number definition has a resolution dependence, such that the Stokes number increases with increasing resolution. We specifically chose 3 and 10 μm dust grains so that the initial conditions were in the St > 1 regime in order to avoid excessively high resolution requirements for the two-fluid method (Laibe and Price, 2012).

Our key findings are below.

1. The PDFs of the gas density are log-normal, as is expected for isothermal, supersonic turbulence. No significant differences are found between the simulations with 3 and 10 μm dust grains, or between the one-fluid and two-fluid methods. This additionally implies that the back-reaction of the dust on the gas has negligible impact on the gas density.

2. Dust density PDFs deviate from log-normal distributions. For both the two-fluid and one-fluid methods, the PDFs peak at values similar to what would be expected from the peak of the gas density PDF shifted by the initial dust-to-gas ratio. If the dust was tightly coupled to the gas, then log-normal distributions would be expected for the dust density PDFs, as they would match the shape of gas density PDFs. Since they do not, this means that dust decouples from

the gas in our calculations. The dust density PDFs for the two-fluid method is broader than for the one-fluid method, suggesting a greater degree of dust decoupling from the gas. The stopping time limiter in the one-fluid method is the primary reason for stronger coupling between gas and dust.

3. We do not find evidence for orders of magnitude increase in the dust-to-gas ratio. PDFs of the dust-to-gas ratio peak at approximately the mean dust-to-gas ratio of 1:100 for both grain sizes and both dust methods. However, the dust-to-gas ratio PDFs are different between the two methods. The two-fluid dust-to-gas ratio PDFs are significantly broader than the one-fluid dust-to-gas ratio PDFs. The maximum dust-to-gas ratio for the one-fluid results is approximately a 3× and 5× increase over the initial ratio for 3 and 10 μm grains, respectively, whereas the two-fluid results reach maximum dust-to-gas ratios of approximately 30× and 39× increase. This means the dust is more tightly coupled to the gas in the one-fluid results.

4. The one-fluid method stopping time limiter avoids spurious dust mass growth due to numerical inaccuracy (see Figure 4.10). Calculations without the limiter exhibit a secondary peak in the dust-to-gas ratio PDFs at extremely low dust-to-gas ratios ($< 10^{-5}$). This low dust-to-gas ratio peak is in excess of the two-fluid PDFs. This behaviour is even more pronounced for 10 μm dust grains compared to 3 μm dust grains, which is consequence of a larger fraction of particles exceeding St > 1. Though necessary to avoid these numerical artefacts

(or instability), the limiter introduces its own numerical artefacts manifesting as enhanced dust-gas coupling.

5. There is reason to be cautious about the dust-to-gas ratio increases obtained with the two-fluid method. The right tail of the dust-to-gas ratio PDFs extends to higher values in the two-fluid method than in the one-fluid method. However, this is the regime where the one-fluid method results are most accurate, as evidenced by the agreement of the right-hand tails of the PDF betweeen the limited and non-limited one-fluid results. This discrepancy raises concerns about potential spurious concentrations arising from the two-fluid approach, especially for particles with $\mathrm{St} < 1$. Such spurious concentrations may occur due to non-adherence of the two-fluid resolution requirement, which, if not adequately met, can lead to artificially high dust concentrations. These artefacts may result from insufficient resolution in capturing the coupled dynamics of dust and gas at smaller scales (inside dense filaments). Note that the turbulent driving force disperses filaments and artificial concentrations over a turbulent crossing time, preventing ongoing accumulation of dust over time.

6. The Stokes number of a particle scales according to $\mathrm{St} \propto \rho^{-2/3}$. This means that changing the numerical resolution affects the Stokes number, as does the adaptive particle resolution with respect to density. Note that even if the numerical requirement around the Stokes number for the one-fluid ($\mathrm{St} < 1$) and the two-fluid ($\mathrm{St} > 1$) is satisfied in the initial conditions, then it may not continued to

be satisfied due to changing dynamical conditions. The correct method should be chosen such that the Stokes number conditions are upheld over the duration of the calculation to avoid numerical artefacts.

Our overall conclusion is that results obtained from simulations of dusty turbulence can be affected by the numerics of the dust solver. The correct dust solver should be chosen based on the Stokes number regime of the dust. If the dust solver is not used in its appropriate Stokes regime, then numerical artefacts can appear as either spurious dust concentrations (exaggerated dust-to-gas ratios) when using the two-fluid method, enhanced coupling of dust and gas when using the one-fluid method with a stopping time limiter, or artificial peaks at low dust-to-gas ratios and dust mass growth for the one-fluid method without limiter. This aligns with the findings of Commerçon et al. (2023), who used a grid-based code for their analysis. In their two-fluid simulations, they observed artificial dust trapping in high-density regions, with the extent of dust enrichment influenced by the resolution of the gas. For their one-fluid simulations, they concluded that while the terminal velocity approximation is well-suited for dust grains smaller than 10μm within dense filaments, it does not accurately capture dust dynamics in low-density regions.

Bibliography

Ballabio, G., G. Dipierro, B. Veronesi, G. Lodato, M. Hutchison, G. Laibe, and D. J. Price: 2018, 'Enforcing dust mass conservation in 3D simulations of tightly coupled grains with the PHANTOM SPH code'. **477**(2), 2766–2771.

Ballesteros-Paredes, J., P. André, P. Hennebelle, R. S. Klessen, J. M. D. Kruijssen, M. Chevance, F. Nakamura, A. Adamo, and E. Vázquez-Semadeni: 2020, 'From Diffuse Gas to Dense Molecular Cloud Cores'. **216**(5), 76.

Bergin, E. A. and M. Tafalla: 2007, 'Cold Dark Clouds: The Initial Conditions for Star Formation'. **45**(1), 339–396.

Bohlin, R. C., B. D. Savage, and J. F. Drake: 1978, 'A survey of interstellar H I from Lalpha absorption measurements. II.'. **224**, 132–142.

Colman, T., N. Brucy, P. Girichidis, S. C. O. Glover, M. Benedettini, J. D. Soler, R. G. Tress, A. Traficante, P. Hennebelle, R. S. Klessen, S. Molinari, and M.-A. Miville-Deschênes: 2024, 'Cloud properties across spatial scales in simulations of the interstellar medium'. **686**, A155.

Commerçon, B., U. Lebreuilly, D. J. Price, F. Lovascio, G. Laibe, and P. Hennebelle: 2023, 'Dynamics of dust grains in turbulent molecular clouds. Conditions for decoupling and limits of different numerical implementations'. **671**, A128.

Dehnen, W. and H. Aly: 2012, 'Improving convergence in smoothed particle hydrodynamics simulations without pairing instability'. **425**(2), 1068–1082.

Draine, B. T.: 2003, 'Interstellar Dust Grains'. **41**, 241–289.

Draine, B. T.: 2011, *Physics of the Interstellar and Intergalactic Medium*.

Eswaran, V. and S. B. Pope: 1988, 'An examination of forcing in direct numerical simulations of turbulence'. *Computers and Fluids* **16**(3), 257–278.

Federrath, C., J. Roman-Duval, R. S. Klessen, W. Schmidt, and M. M. Mac Low: 2010, 'Comparing the statistics of interstellar turbulence in simulations and observations. Solenoidal versus compressive turbulence forcing'. **512**, A81.

Goodman, A. A., J. E. Pineda, and S. L. Schnee: 2009, 'The "True" Column Density Distribution in Star-Forming Molecular Clouds'. **692**(1), 91–103.

Habart, E., M. Walmsley, L. Verstraete, S. Cazaux, R. Maiolino, P. Cox, F. Boulanger, and G. Pineau des Forêts: 2005, 'Molecular Hydrogen'. **119**(1-4), 71–91.

Hopkins, P. F.: 2015, 'A new class of accurate, mesh-free hydrodynamic simulation methods'. **450**(1), 53–110.

Hopkins, P. F. and H. Lee: 2016, 'The fundamentally different dynamics of dust and gas in molecular clouds'. **456**(4), 4174–4190.

Kong, S., C. J. Lada, E. A. Lada, C. Román-Zúñiga, J. H. Bieging, M. Lombardi, J. Forbrich, and J. F. Alves: 2015, 'The Relationship between the Dust and Gas-Phase CO across the California Molecular Cloud'. **805**(1), 58.

Kwok, S.: 1975, 'Radiation pressure on grains as a mechanism for mass loss in red giants.'. **198**, 583–591.

Lada, C. J. and T. M. Dame: 2020, 'The Mass-Size Relation and the Constancy of GMC Surface Densities in the Milky Way'. **898**(1), 3.

Lada, C. J., E. A. Lada, D. P. Clemens, and J. Bally: 1994, 'Dust Extinction and Molecular Gas in the Dark Cloud IC 5146'. **429**, 694.

Laibe, G. and D. J. Price: 2012, 'Dusty gas with smoothed particle hydrodynamics - I. Algorithm and test suite'. **420**(3), 2345–2364.

Larson, R. B.: 1981. *MNRAS* **194**, 809–826.

Lattanzio, J. C., J. J. Monaghan, H. Pongracic, and M. P. Schwarz: 1984, 'Cloud-cloud collisions'. **5**(4), 495–498.

Lewis, J. A., C. J. Lada, and T. M. Dame: 2022, 'Systematic Investigation of Dust and Gaseous CO in 12 Nearby Molecular Clouds'. **931**(1), 9.

Liseau, R., B. Larsson, T. Lunttila, M. Olberg, G. Rydbeck, P. Bergman, K. Justtanont, G. Olofsson, and B. L. de Vries: 2015, 'VizieR Online Data Catalog: Gas and dust in the star-forming region rho OphA (Liseau+, 2015)'. VizieR On-line Data Catalog: J/A+A/578/A131. Originally published in: 2015A&A...578A.131L.

Mathis, J. S., W. Rumpl, and K. H. Nordsieck: 1977, 'The size distribution of interstellar grains.'. **217**, 425–433.

Mattsson, L., A. Bhatnagar, F. A. Gent, and B. Villarroel: 2019a, 'Clustering and dynamic decoupling of dust grains in turbulent molecular clouds'. **483**(4), 5623–5641.

Mattsson, L., J. P. U. Fynbo, and B. Villarroel: 2019b, 'Small-scale clustering of nano-dust grains in supersonic turbulence'. **490**(4), 5788–5797.

Passot, T. and E. Vázquez-Semadeni: 1998, 'Density probability distribution in one-dimensional polytropic gas dynamics'. **58**(4), 4501–4510.

Pineda, J. E., P. Caselli, and A. A. Goodman: 2008, 'CO Isotopologues in the Perseus Molecular Cloud Complex: the X-factor and Regional Variations'. **679**(1), 481–496.

Price, D. J. and G. Laibe: 2015, 'A fast and explicit algorithm for simulating the dynamics of small dust grains with smoothed particle hydrodynamics'. **451**(1), 813–826.

Price, D. J., J. Wurster, T. S. Tricco, C. Nixon, S. Toupin, A. Pettitt, C. Chan, D. Mentiplay, G. Laibe, S. Glover, C. Dobbs, R. Nealon, D. Liptai, H. Worpel, C. Bonnerot, G. Dipierro, G. Ballabio, E. Ragusa, C. Federrath, R. Iaconi, T. Reichardt, D. Forgan, M. Hutchison, T. Constantino, B. Ayliffe, K. Hirsh, and G. Lodato: 2018, 'Phantom: A Smoothed Particle Hydrodynamics and Magnetohydrodynamics Code for Astrophysics'. **35**, e031.

Scalo, J., E. Vázquez-Semadeni, D. Chappell, and T. Passot: 1998, 'On the Probability Density Function of Galactic Gas. I. Numerical Simulations and the Significance of the Polytropic Index'. **504**(2), 835–853.

Schmidt, W., C. Federrath, M. Hupp, S. Kern, and J. C. Niemeyer: 2009, 'Numerical simulations of compressively driven interstellar turbulence. I. Isothermal gas'. **494**(1), 127–145.

Schneider, N., S. Bontemps, R. Simon, V. Ossenkopf, C. Federrath, R. S. Klessen, F. Motte, P. André, J. Stutzki, and C. Brunt: 2011, 'The link between molecular cloud structure and turbulence'. **529**, A1.

Snow, T. P. and B. J. McCall: 2006, 'Diffuse Atomic and Molecular Clouds'. **44**(1), 367–414.

Solomon, P. M., A. R. Rivolo, J. Barrett, and A. Yahil: 1987, 'Mass, Luminosity, and Line Width Relations of Galactic Molecular Clouds'. **319**, 730.

Solomon, P. M., N. Z. Scoville, and D. B. Sanders: 1979, 'Giant molecular clouds in the Galaxy: the distribution of ^{13}CO emission in the galactic plane.'. **232**, L89–L93.

Stepinski, T. F. and P. Valageas: 1996, 'Global evolution of solid matter in turbulent protoplanetary disks. I. Aerodynamics of solid particles.'. **309**, 301–312.

Teyssier, R.: 2002, 'Cosmological hydrodynamics with adaptive mesh refinement: A new high resolution code called RAMSES'. *Astronomy amp; Astrophysics* **385**(1), 337–364.

Tricco, T. S., D. J. Price, and G. Laibe: 2017, 'Is the dust-to-gas ratio constant in molecular clouds?'. **471**(1), L52–L56.

Vazquez-Semadeni, E.: 1994, 'Hierarchical Structure in Nearly Pressureless Flows as a Consequence of Self-similar Statistics'. **423**, 681.

Youdin, A. N. and J. Goodman: 2005, 'Streaming Instabilities in Protoplanetary Disks'. **620**(1), 459–469.